JVST B
Journal of Vacuum Science & Technology B

Strain-dependent luminescence and piezoelectricity in monolayer transition metal dichalcogenides

Cite as: J. Vac. Sci. Technol. B **38**, 042205 (2020); https://doi.org/10.1116/6.0000251
Submitted: 09 April 2020 . Accepted: 18 June 2020 . Published Online: 06 July 2020

Alex C. De Palma, Gabriel Cossio, Kayleigh Jones, Jiamin Quan, Xiaoqin Li, and Edward T. Yu

JVST B
Journal of Vacuum Science & Technology B

ARTICLE

avs.scitation.org/journal/jvb

Strain-dependent luminescence and piezoelectricity in monolayer transition metal dichalcogenides

Cite as: J. Vac. Sci. Technol. B 38, 042205 (2020); doi: 10.1116/6.0000251
Submitted: 9 April 2020 · Accepted: 18 June 2020 ·
Published Online: 6 July 2020

View Online Export Citation CrossMark

Alex C. De Palma,[1] Gabriel Cossio,[1] Kayleigh Jones,[2] Jiamin Quan,[2] Xiaoqin Li,[2] and Edward T. Yu[1,a)]

AFFILIATIONS

[1]Microelectronics Research Center, The University of Texas at Austin, Austin, Texas 78758
[2]Department of Physics, The University of Texas at Austin, Austin, Texas 78712

Note: This paper is part of the Special Topic Collection from the 47th Conference on the Physics and Chemistry of Surfaces and Interfaces (PCSI-47) 2020 meeting.
[a)]**Electronic mail:** ety@ece.utexas.edu

ABSTRACT

The modification of optical and electronic properties of transition metal dichalcogenides via mechanical deformation has been widely studied. Their ability to withstand large deformations before rupture has enabled large tunability of the bandgap, and further, the spatially varying strain has been shown to control the spatial distribution of the bandgap and lead to effects such as carrier funneling. Monolayer transition metal dichalcogenides exhibit a significant piezoelectric effect that could couple to a spatially inhomogeneous strain distribution to influence electronic and optical behavior. We investigate both experimentally and theoretically an example case of photoluminescence in structures with a strain distribution similar to that employed in single-photon emitters but generated here via nanoindentation. Using a mechanical model for strain induced by nanoindentation, we show that piezoelectricity can result in charge densities reaching 10^{12} e/cm^2 and can generate electrostatic potential variations on the order of ±0.1 V across the suspended monolayer. We analyze the implications of these results for luminescence and exciton transport in monolayer transition metal dichalcogenides with spatially varying strain.

I. INTRODUCTION

Transition metal dichalcogenides (TMDs) are a class of layered materials that can be isolated into atomically thin layers. TMDs existing in the trigonal prismatic 2H phase, such as MoS_2, WS_2, $MoSe_2$, and WSe_2, are semiconducting and have shown a number of interesting properties, such as large exciton binding energies[1] and the ability to withstand large mechanical deformations before rupture.[2] Additionally, the properties of these materials can be significantly modified in a number of ways, such as stacking, defects, and strain. Strain in atomically thin TMDs has a broad range of consequences and can be used for tuning of their optical and electronic properties.[3–7] In particular, the use of localized strain to engineer these properties has generated a variety of effects, such as carrier funneling,[8–11] and has been strongly associated with the observation of single-photon emission in TMD materials.[12–16] Additionally, TMDs exhibit intrinsic piezoelectricity in monolayer and few-layer form originating from a lack of centrosymmetry with odd number of layers.[17–20] The presence of piezoelectricity in TMD systems with strain and strain gradients can have appreciable effects on electronic and optical behavior analogous to those observed in III-V compound semiconductors,[21–27] which in TMD materials have only begun to be explored.[20,28,29] Understanding these effects is necessary for the engineering of TMD-based structures in which strain is present.

In this work, we explore the effects of piezoelectricity in monolayer MoS_2 and WSe_2 in the presence of strain and strain gradients, considering an example geometry of a thin monolayer TMD suspended over a circular hole and indented by a spherical nanoindenter. We first model the strain distribution for this geometry according to the mechanics of a spherical indenter in frictionless contact with a membrane to calculate the piezoelectric-induced electrostatic potential. Monolayer MoS_2 and WSe_2 suspended over circular holes were deformed via atomic force microscope (AFM)

indentation, and room-temperature photoluminescence (PL) measurements were simultaneously performed as a function of indentation force to determine the effects of the localized strain on exciton bandgap and exciton diffusion. Additionally, we show through calculations that spatially varying strain can be a source of electrostatic potentials due to the piezoelectric effect that may influence the motion of charge carriers and the spatial distribution of carrier recombination.

II. EXPERIMENT

To create TMD monolayers suspended over voids for nanoindentation experiments, a hexagonal array of holes was first etched into a SiO_2/Si substrate using a nanosphere lithography process.[30–34] Polystyrene spheres 2000 nm in diameter were deposited onto the substrate in a close-packed monolayer before being etched down to ~800 nm diameter. A Cr layer was then deposited using e-beam evaporation, the spheres were removed in toluene, and the SiO_2 was etched in the gaps in the Cr mask left behind by the spheres. All etching steps were performed using reactive ion etching. The period of the hexagonal array of holes was 2000 nm, and the final hole dimensions were approximately 800 nm in diameter and 300 nm in depth. For each sample, MoS_2 or WSe_2 was exfoliated from bulk crystal and transferred onto the nanopatterned substrates via a viscoelastic dry stamping method using polydimethylsiloxane (PDMS).[35] The exfoliated flakes shown in Fig. 1(a) consist of regions of varying

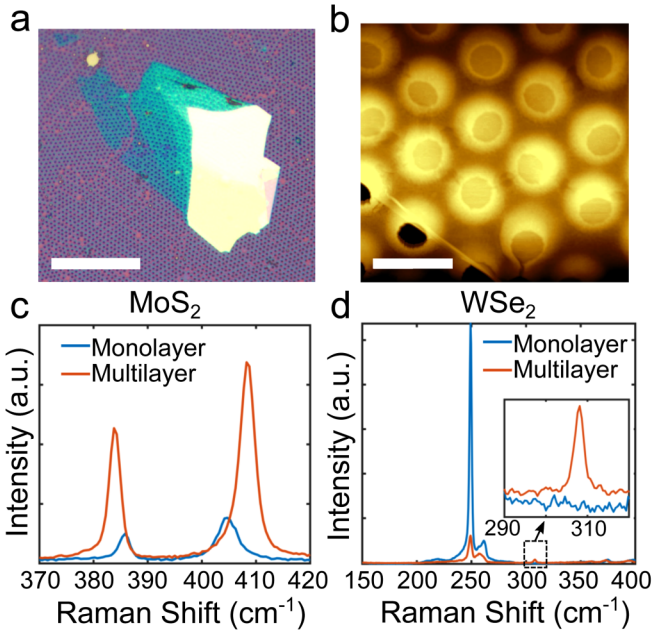

FIG. 1. (a) Optical image of the exfoliated MoS_2 flake transferred onto the nanopatterned substrate. The scale bar corresponds to 40 μm. (b) Tapping mode AFM scan of MoS_2 monolayer transferred onto the nanopatterned substrate, where the scale bar equals 2 μm. (c) Raman spectroscopy measurements of transferred MoS_2 and (d) WSe_2. The inset of (d) is a magnification of the WSe_2 Raman spectra near 300 cm^{-1}.

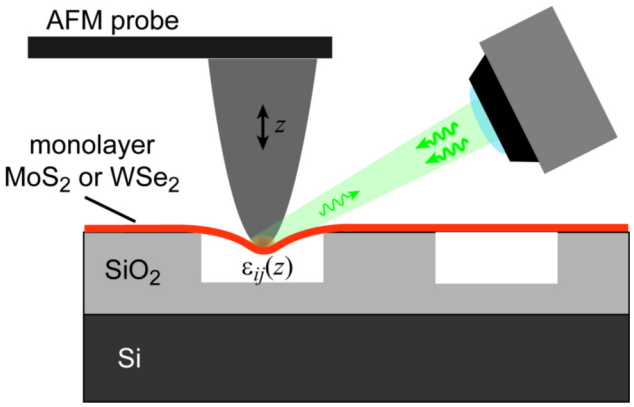

FIG. 2. Schematic diagram of the indentation experiment and the side-illumination configuration for PL measurements.

layer thickness. AFM scans [Fig. 1(b)] confirm that the transferred monolayers are suspended over multiple individual holes. Raman spectroscopy [Figs. 1(c) and 1(d)] is used to determine the regions of monolayer material in both flakes. For MoS_2, layer number is determined from the separation between the E^1_{2g} and A_{1g} peaks, which decreases with decreasing layer number. The monolayer region is confirmed based on a peak separation of 19 cm^{-1}, which is consistent with other studies.[36,37] For WSe_2, monolayer regions are identified by the lack of a multilayer peak at ~308 cm^{-1} in the Raman spectra.[38,39] This peak is generally observed in WSe_2 consisting of two or more layers and can be assigned to the normally optically inactive B_{2g} mode.[39]

Si AFM tips (OPUS 160NG) with tip radii of ~7 nm (manufacturer specification) are used to indent monolayer regions of MoS_2 and WSe_2. Spring constants are determined via the Sader method[40] to range from 5 to 25 N/m. Additional tips with larger radius were created by coating Si tips with SiO_2 via e-beam evaporation with the resulting tip radii ranging between 30 and 50 nm. The indentation was performed by pressing the AFM tip into the suspended monolayer at increments of 5–10 nm sample displacement while simultaneously measuring the deflection of the cantilever. During indentation, PL measurements were performed with a 532 nm laser excitation in the side-illumination configuration, illustrated in Fig. 2. In this configuration, an excitation laser focused with a 100× objective illuminates the sample at an incident angle of 60°. The laser spot size is estimated to be 500 nm in the focal plane of the objective. We approximate the laser spot projected onto the sample as an ellipse with a major axis of 1000 nm and minor axis of 500 nm due to the angle of incidence of the objective. PL measurements were performed at each indentation depth at a power of 0.1 mW and exposure time of 10 s.

III. MODELING

A. Mechanics of nanoindentation of monolayer TMDs

Calculations of the strain distribution were performed according to Foppl–Hencky membrane theory,[41,42] which is appropriate

for 2D TMDs due to their negligible bending stiffness. We follow the model of a spherical indenter in frictionless contact with a clamped circular membrane in order to describe the AFM indentation experiment, using an approach consistent with that of Bhatia and Nachbar.[43] Their method is to calculate solutions by assuming two regions: the constrained region in frictionless contact with the spherical indenter and the free region of the surrounding membrane. This allows for consideration of the finite size of the indenter and yields closed form solutions that describe the strain in the region near the indenter, unlike other methods such as the Schwerin solution,[44] which calculates infinite strain but finite deflections at the point of indentation. Other works have expanded on this approach by developing approximate[45] and exact[46] methods valid at a broader range of indentation loads; however, the indentation loads used in this work fall within the range of Bhatia and Nachbar's method.[43] The main feature of the calculation is to assume the constrained region is deformed according to the spherical profile of the indenter. Radial stress is continuous across the boundaries, both between the free and constrained regions as well as the free region and the outer boundary, and the stress is entirely radial in the free region. For our calculations, we assume pretension of 1 N/m in the membrane for both WSe_2 and MoS_2, which is approximately consistent with our experimental indentation data. The Poisson ratio and elastic modulus, respectively, are taken to be 0.27 [Ref. 47] and 270 GPa [Ref. 2] for MoS_2 and 0.19 [Ref. 48] and 167 GPa [Ref. 49] for WSe_2.

The strain distributions in the mechanical model are calculated in terms of a radial and a circumferential component of tensile strain. The components of strain at a given point are defined according to the local radial and circumferential directions referenced between the center of indentation and the given point, as shown in Fig. 3(a). The solution for the strain distribution is radially symmetric; however, for calculations of piezoelectricity, the x and y axes are defined as lying along with orthogonal armchair and zigzag directions of the lattice, respectively.

An example of the radial and circumferential strain distribution due to indentation is shown in Fig. 3(b). The strain is in-plane hydrostatic at the very center but transitions toward uniaxial along the radial direction away from the center of indentation. The strain is mostly confined to the point of indentation, creating large strain gradients that could interact with the piezoelectric nature of these TMDs. Increasing the radius of the indenter has the effect of broadening the strain distribution, as shown in Fig. 3(c). The relationship between indentation force, maximum strain, and tip radius for MoS_2 calculated with the mechanical model is shown in Fig. 3(d). There is a nonlinear relationship between force and strain, and the strain at a given indentation force depends significantly on the indenter radius. In Fig. 3(d), results are not shown for indentation load $F < 10$ nN since the method of Bhatia and Nachbar is only valid when $F \gg \sim 10$ nN.

B. Calculation of piezoelectricity

To a first approximation, we can consider the direct piezoelectric effect as the generation of polarization via strain with the

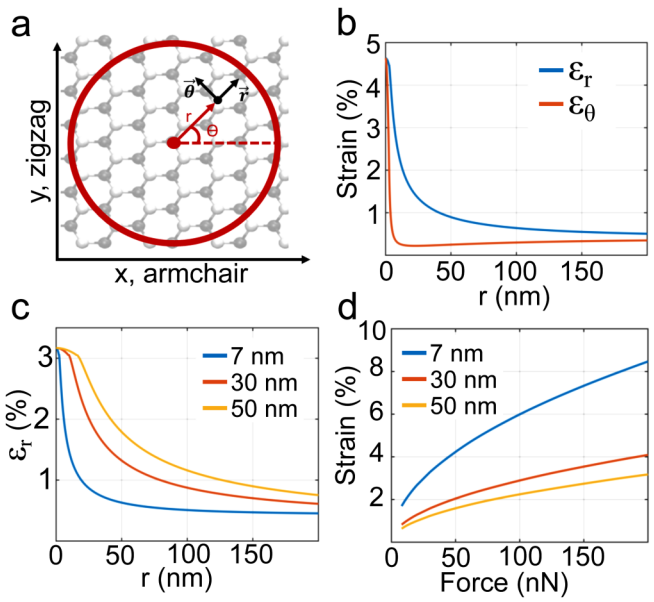

FIG. 3. (a) Diagram of the coordinate systems referenced in the modeling of indentation and piezoelectricity. The x-y coordinate system refers to the armchair and zigzag directions of the TMD lattice, while the r–θ coordinate system refers to the local radial and circumferential directions at the point defined by r and θ, where r is referenced to the center of indentation. (b) Comparison of the radial and circumferential strain with respect to r for a 7 nm indenter applying a 60 nN load to monolayer MoS_2. (c) Dependence of the calculated radial strain distribution on the indenter radius for monolayer MoS_2. The indentation load is 28, 120, and 200 nN for 7, 30, and 50 nm indenters, respectively. (d) The relationship between indentation force, the maximum strain generated at the center of indentation, and the indenter radius, calculated for monolayer MoS_2.

following equation:

$$P_i = e_{ij}\varepsilon_j, \tag{1}$$

where P is the polarization, e is the piezoelectric tensor, and ε is the strain in Voigt notation in reference to the x-y coordinate system, which can be derived from the strain components in the local coordinate system of the mechanical model via a rotation. The piezoelectric tensor for monolayer MoS_2 and WSe_2 is determined by their D_{3h} point group,

$$e = \begin{pmatrix} e11 & -e11 & 0 & 0 & 0 & 0 \\ 0 & 0 & 0 & 0 & 0 & -e11 \\ 0 & 0 & 0 & 0 & 0 & 0 \end{pmatrix}. \tag{2}$$

As can be seen from Eq. (2), the piezoelectric effect in these materials depends on only one unique value for the coefficients, e11. The values used in our calculations for MoS_2 and WSe_2 are 3.6E–10 and 2.7E–10 C/m, which were calculated in previous work using density functional theory (DFT).[17] Experimental studies have measured piezoelectric coefficient for monolayer MoS_2 to be 2.9E–

10 C/m[19], smaller than the DFT value; however, we use the value from Ref. 17 for a consistent comparison between TMDs.

We can also account for the effects of flexoelectricity from the strain distribution. Flexoelectricity is the generation of a polarization field by a strain gradient,

$$P_k = \mu_{ijkl} \frac{\partial \varepsilon_{ij}}{\partial x_l}, \tag{3}$$

where μ_{ijkl} is the flexoelectric coefficient and $\frac{\partial \varepsilon_{ij}}{\partial x_l}$ is the derivative of the ε_{ij} component of strain in the x_l direction. While the flexoelectric coefficients are not precisely known, their magnitudes can be roughly estimated by Kogan's estimation,[50] which has been found to agree experimentally with the out of plane effective flexoelectric coupling strengths for TMDs,[51,52]

$$\mu \approx \frac{q\chi}{4\pi\epsilon_o a}, \tag{4}$$

where q is the elementary charge, a is the lattice constant, and χ is the electric susceptibility. Using Eq. (4), we obtain an estimate for the flexoelectric coefficient of 1.4E–10 C/m, or ~1E–19 C normalized to the TMD monolayer thickness for WSe_2, and the ratio of the flexoelectric coefficient to the piezoelectric coefficient is 1E–9. Therefore, for the flexoelectric effect to be comparable to the piezoelectric effect, the required ratio of the strain gradient to the strain would need to be 1E9. Considering as an example the strain distribution from Fig. 3(b), which corresponds to a sharp 7 nm indenter generating large strain gradients, the calculated ratio of the maximum strain gradient to the maximum strain is only ~1E8. Thus, the flexoelectric generation of polarization is about an order of magnitude smaller than the piezoelectric contribution, even in an extreme case of large strain gradients originating from the sharpest indenter in our experiments. Though flexoelectricity can make a sizable contribution in the case of the sharpest indenter, piezoelectricity is still the dominant form of electromechanical coupling for the geometries considered here. For this reason, and due to uncertainty in the values of the flexoelectric coefficients, we exclude the flexoelectric effect from further calculations.

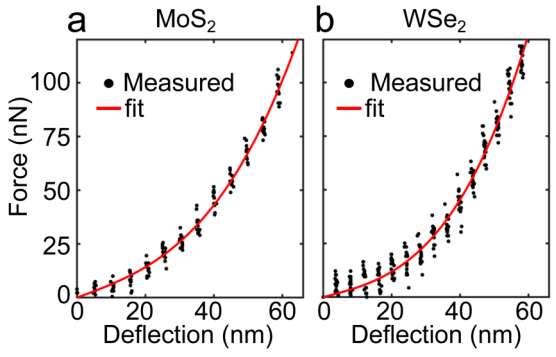

FIG. 4. F-d curves measured during AFM indentation with a tip radius of 7 nm for monolayer (a) MoS_2 and (b) WSe_2.

The polarization generated by piezoelectricity can result in bound charges when a nonzero divergence of the polarization is present, given by the following relation:

$$\sigma_b = -\nabla \cdot P. \tag{6}$$

Since the polarization is proportional to the strain, spatially varying strain will in many cases generate a bound charge density. The magnitude and distribution of the bound charges, and any electrostatic effects that may result from them, are highly dependent on not only the strain but also the strain distribution. The electrostatic potential and field distribution originating from these bound charges are calculated using custom MATLAB code utilizing the method of moments.[53] We assume the bound charges present in suspended monolayer TMDs are approximated by a two-dimensional sheet charge in air while neglecting the dielectric constant of the monolayer and the out of plane displacement of the membrane. Additional finite-element numerical calculations performed using COMSOL are in very good agreement with the MATLAB calculations.

IV. RESULTS AND DISCUSSION

A. Experimental nanoindentation results

To verify that suspended MoS_2/WSe_2 behaves as a nonlinear membrane under AFM indentation, we fit the force-deflection (F-d) curves to the F-d relationship[54] of a nonlinear membrane suspended over a circular hole,

$$F = \sigma_o^{2D} \pi d + E^{2D} \frac{q^3 d^3}{r^2}, \tag{7}$$

where σ_o^{2D} is the prestress normalized by membrane thickness, d is the vertical deflection of the membrane at the center, E^{2D} is the elastic modulus normalized by the membrane thickness, r is the radius of the hole over which the membrane is suspended, and q is a dimensionless parameter derived from Poisson's ratio, ν: $q = 1/(1.05 - 0.15\nu - 0.16\nu^2)$. Example F-d curves for MoS_2/WSe_2 (Fig. 4) show that the relationship between force and deflection is well approximated by Eq. (7). From these curves, we extract a value for the 2D elastic modulus for MoS_2/WSe_2 of 160 ± 30 and 80 ± 35 N/m, respectively, comparable to the literature values for these materials derived by similar methods of indentation.[2,49] These results were repeatable with multiple indentation measurements over the same hole with suspended TMD monolayers. The F-d results indicate that the suspended TMD monolayers behave as nonlinear membranes in these experiments and can be well approximated by the mechanical model used here.

The photoluminescence spectra shown in Fig. 5 were measured during indentation and reveal a modest redshift in the dominant luminescence feature which increases with increasing indentation force. At small indentation forces, taking the difference between the PL spectra at 0 nN [Fig. 6(a)] and the spectra at nonzero indentation forces, we observe a small side peak for the 50 nm tip indenting WSe_2, as shown in Figs. 6(b)–6(d). Though these small forces fall outside the regime of the mechanical model's reliability, we can still roughly estimate the maximum strain using

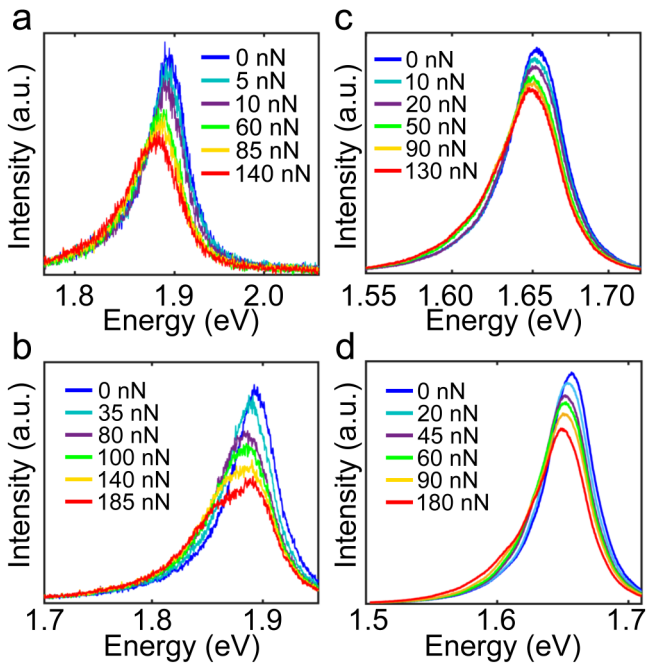

FIG. 5. (a) PL spectra as a function of indentation load for monolayer MoS_2 using a 7 nm AFM tip and a (b) 50 nm tip. (c) PL spectra as a function of indentation load for monolayer WSe_2 using a 7 nm tip and a (d) 50 nm AFM tip.

this model. The strain predicted by the energy of the side peak depends on the assumed gauge factor of the exciton bandgap. The experimental value for the WSe_2 gauge factor from Ref. 3, 60 meV/%, implies a slightly larger strain than the strain beneath the indenter predicted by the model; however, theoretical calculations[3,5,7] suggest that the value of the gauge factor could be closer to ~110–130 meV/%. As shown in Fig. 6(h), the strain calculated via the mechanical model falls between the strain from the side peak shifts implied by the two different gauge factors, and the trend in force versus strain qualitatively agrees between the PL measurements and the model. These observations imply that the PL emission features in Figs. 6(b)–6(d) originate from excitons near the center of indentation. The amplitude of the peaks is ~1% that of the unstrained peak, and at biaxial strains beyond 1.2% (indentations above 20 nN), these side peaks are no longer observed. This side peak is not observed in WSe_2 indentation measurements with a small tip nor is it seen in MoS_2 for any tip size or indentation force.

The PL signal at larger loads consists of an inhomogeneous broadening, which can be modeled with a slightly redshifted main peak and a more significantly redshifted secondary peak [Figs. 6(e)–6(g)]. We attribute the slightly redshifted main peak to a laser spot size which is comparable to but larger than the region encompassed by carrier funneling, resulting in portions of the PL signal originating from relatively unstrained regions outside of the funneling region. The main peak for MoS_2 is modeled using two pseudo-Voigt peaks to account for the presence of trions at room temperature[55] while trions are not found in the PL spectrum of WSe_2 at room temperature.[56] The secondary peak is consistently at ~1.62 eV in WSe_2, 40 meV below the unstrained PL peak, regardless of tip size or indentation force. With increasing indentation force, the intensity of the secondary peak increases with only a modest redshift in peak position, and the intensity of the main peak decreases with indentation force, also with a modest redshift in peak position. Similarly, for MoS_2, the side peak emerges around 1.86 eV, 30 meV below the unstrained peak, regardless of tip size. The exciton peaks for WSe_2 and MoS_2 have been shown to decrease by, respectively, ~60 and ~50 meV/% with increasing biaxial tensile strain in previous PL experiments.[3] This would imply a level of strain observed in the secondary peak at large indentation loads of 0.5%–1% for both materials, depending on whether the strain is uniaxial or biaxial. This is significantly less than the amount of strain being induced via indentation during these PL measurements based on the applied indentation load. While carrier funneling could affect the relative population of excitons and trions in both TMDs due to an increased carrier density, PL originating from both trions and excitons redshifts with tensile strain at comparable rates.[57] At these larger indentation loads, there is no PL feature between the main peak and the secondary peak that correlates to exciton recombination near the center of indentation.

Since tensile strain increases gradually from the edge to the center of the suspended TMDs upon indentation, the bandgap and exciton resonance energy are expected to be lowest near the center, which has been previously shown to result in carrier funneling toward the region of largest strain.[8–11] Though the spot size of the laser in our measurement is comparable to the size of the hole and is larger than the region of highest strain, carrier funneling would be expected to lower the energy of recombination of a significant number of excitons within the optically averaged area of the excitation laser spot. To estimate the drift length of the excitons in the strain field, we can use the following relation:[8]

$$l_{drift} = \langle v \rangle_{drift} \tau_{1/2} = \frac{\nabla E_{exc}}{m_{exc}} \tau_{dephase} \tau_{1/2}, \quad (8)$$

where ∇E_{exc} is the gradient of the exciton resonance energy, m_{exc} is the exciton mass, $\tau_{dephase}$ is the phase relaxation time, and $\tau_{1/2}$ is the exciton lifetime. The funnel radius can be defined as the farthest point from the center at which the drift length of the excitons is sufficient to reach the center of indentation. We can estimate the drift length at a given point via Eq. (8) using the exciton energy gradient derived from the strain gradient at that point. Using this method, and parameters for MoS_2 from Ref. 8, we calculate an exciton funneling radius ranging from 80 and 190 nm for the fast and slow decay components at an indentation load of 8 nN, to 300 nm and 800 for the fast and slow decay components at an indentation load of 200 nN. The funneling radius is significant, even at small indentation loads, which is consistent with the PL peaks observed in Figs. 6(b)–6(d). Exciton funneling should become more pronounced at larger indentation loads based on the calculated drift length; what is instead observed is a complete vanishing of the side peak above 20 nN. A direct-indirect bandgap transition occurring with increasing tensile strain has been

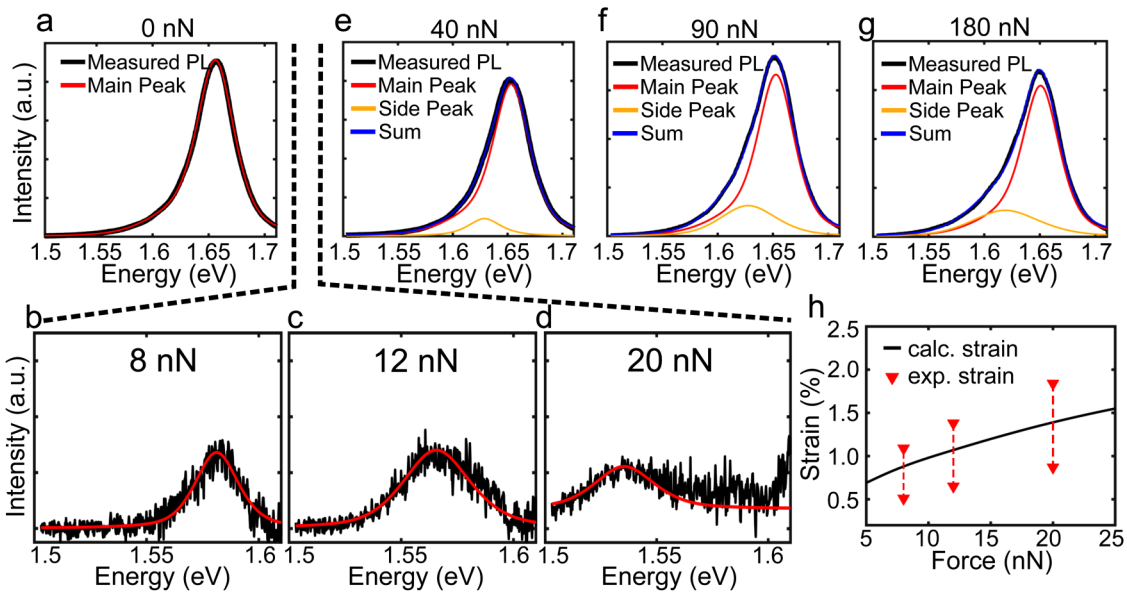

FIG. 6. (a) Unstrained PL spectrum and its fitting. (b)–(d) Fittings of the PL spectra at small loads for WSe_2 and a 50 nm indenter radius. The plotted intensity is the difference between the PL spectrum at a given indentation force and the unstrained PL spectrum. The black and red lines correspond to the measured PL and the fit, respectively. Each peak was fit to a pseudo-Voigt function. (e)–(g) PL fitting at larger indentation loads, consisting of a main peak which is assumed to have a peak shape equal to the PL peak at 0 nN, and a side peak which is modeled using a pseudo-Voigt function. The sum peak is the sum of the main peak and the side peak. (h) Strain vs indentation force calculated from the mechanical model is compared to the strain implied by the peak position in (b)–(d). The top and bottom lines of the "exp. strain" plot use the experimental and theoretical A exciton gauge factor from Ref. 3 (upper data points) and Refs. 3, 5, and 7 (lower data points), respectively.

observed in PL studies of MoS_2,[5,6] which could contribute to the lack of redshifted PL signal at both small and large indentation loads. While there is also a direct-indirect transition in WSe_2, the bandgap remains direct up to 2%–4% biaxial tensile strain,[7,58] corresponding to an indentation-induced direct-indirect transition between 80 nN and over 200 nN for the 50 nm indenter—greater than the force at which the side peak vanishes. While the lack of redshifted PL signal could be attributed to the indirect transition at larger loads, the consistency of the results between 40 and 180 nN for WSe2 [Figs. 6(e)–6(g)], which are below and potentially above the direct-indirect transition respectively, suggests that the indirect transition does not play a significant factor in the observed PL spectra of WSe_2 with the 50 nm indenter. The small magnitude of the side peak in WSe_2, along with its complete disappearance at strains above 1.5%, suggests a suppression of the PL in the regions of larger strain near the indenter, which increases with the overall level of strain. As we will discuss further in the following sections, these results could point to interference in the carrier funneling effect due to piezoelectricity.

B. Modeled piezoelectric potential during indentation

An example of the distribution of polarization and bound charge during indentation is shown in Fig. 7. The radially symmetric strain produces a threefold symmetry of the polarization reflecting the threefold symmetry of the lattice. Armchair directions connecting the center of indentation to hole edge exhibit polarization also along with the armchair directions, resulting in maximum bound charge. Polarization along with the zigzag directions between the center of indentation and hole edge also generates a polarization in the armchair direction, and hence zero bound charge. The bound charge density reaches as high as 10^{12} e/cm^2, which results in variation in the electrostatic potential on the order of ±0.1 V. The potential variation shares the same threefold symmetry as the bound charge and polarization, and the largest magnitude of electrostatic potential is located around but not at the point of highest strain.

The relationship between the strain, charge density, potential, and indenter radius is shown in Fig. 8. Both the charge density and potential increase with increasing maximum strain. In the case of increasing tip radius, the charge density decreases while the maximum potential variation remains relatively constant. Figures 8(c) and 8(d) show the relationship between the indenter radius and the distribution of the electrostatic potential. Increasing indenter radius causes the distribution of the potential to spread out with the maximum absolute value of the potential occurring at a larger distance from the center.

The electrostatic potential due to piezoelectricity should rigidly shift the local band edge energies by an amount equal to the potential energy. While effects of mobile carrier distributions are not considered explicitly here, typical electronic densities of states for TMD monolayers suggest that shifts in band edge energies in the presence of mobile carriers should be comparable to those computed here. Figures 9(a) and 9(b) show the spatial distribution

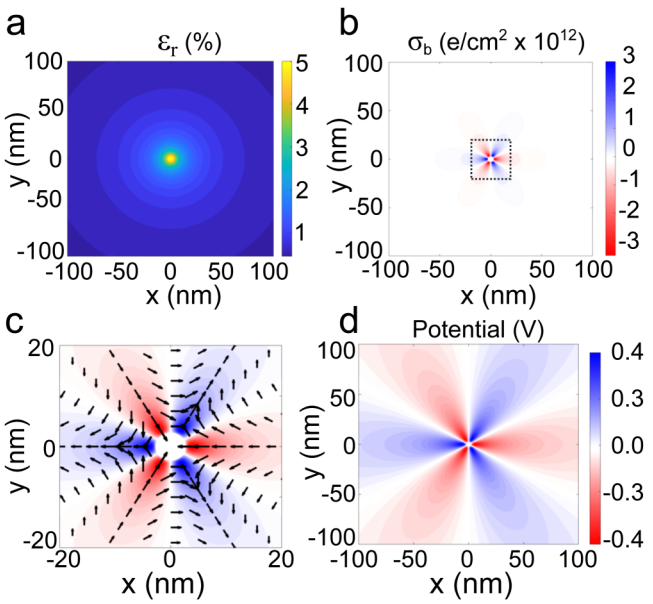

FIG. 7. Summary results for 60 nN indentation of monolayer MoS_2 using a 7 nm indenter radius. (a) The spatial distribution of the radial component of strain. (b) The bound charge density calculated from the strain distribution in (a). (c) The polarization vector field which generates bound charges. The arrows represent the polarization while the coloring corresponds to the charge density shown in the marked area of (b). (d) The electrostatic potential resulting from the bound charge density shown in (b).

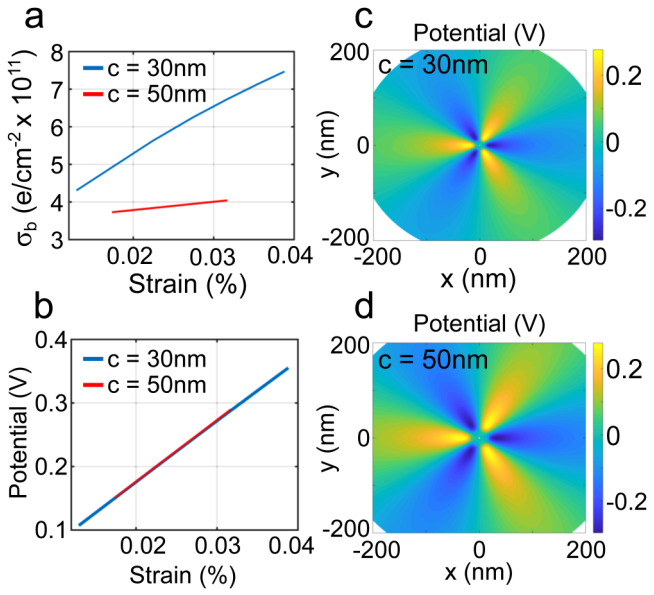

FIG. 8. Dependence of calculated quantities involving piezoelectricity on indenter radius, c, for monolayer MoS_2. (a) Relationship between the maximum value of the bound charge density and maximum strain generated during indentation. (b) Dependence of the maximum value of potential over the monolayer on the maximum value of strain. The potential distributions for 30 and 50 nm indenters are shown in (c) and (d), respectively. The indentation load was chosen such that the maximum strain is the same in both cases, 3.2%.

of the conduction band minimum (CBM) and valence band maximum (VBM) for the case of indented WSe_2 considering strain deformation potentials alone. The change in band edge energies is assumed to relate to the elements of the strain tensor in the following way:

$$E_k^{CB} = E_o^{CB} + a_k^{CB\star}(\varepsilon_r + \varepsilon_\theta), \tag{9}$$

$$E_k^{VB} = E_o^{VB} + a_k^{VB\star}(\varepsilon_r + \varepsilon_\theta), \tag{10}$$

where E_k^{CB} and E_k^{VB} are the energies of the conduction and valence band edges at the K-point, respectively, and a_k^{CB} and a_k^{VB} are the uniaxial deformation potentials of the conduction and valence bands for WSe_2, respectively. The values for a_k^{CB} and a_k^{VB} are taken from the deformation potentials in the zigzag direction,[59] −6.03 and −0.16 eV, respectively. The uniaxial deformation potentials in Ref. 59 are nearly equal in both the armchair and zigzag directions, allowing for the deformation potentials to be approximated as isotropic, and the use of the strain components in the local coordinate system, ε_r and ε_θ. Equations (8) and (9) reasonably reproduce the deformation potentials in the uniaxial and biaxial limits and can approximate between the two regimes. In the limit where one of ε_r or ε_θ is equal to zero, the expression exactly reproduces the deformation potential for uniaxial deformation calculated in Ref. 59. In the biaxial limit, where ε_r and ε_θ are equal, the effective deformation potential is 117 meV/%, comparable to previous theoretical results.[3,5,7]

The exciton funneling mechanism discussed in the literature is often depicted similarly to Figs. 9(a) and 9(b): a spatially varying strain distribution steadily decreases the optical bandgap as the point of largest tensile strain is approached. However, this picture does not include any piezoelectric effects that might also arise from the strain distribution. If we include piezoelectric effects via the corresponding electrostatic potential [Figs. 9(c)–9(f)], then the spatial distribution of the CBM and VBM is significantly altered. Instead of the bandgap minimum lying at the center, where the highest tensile strain is present, the minimum of the CBM and maximum of the VBM lie at different points, both some distance away from the center. In the case of free carriers, electrons and holes would be funneled to different positions in the monolayer, which could affect the rate of carrier recombination. In the case of excitons that are relevant to PL experiments in TMDs, electrons and holes are bound together, and the funneling picture becomes complicated as electrons and holes experience forces drawing them to separate locations in the monolayer. If these forces, i.e., the electrostatic field, are strong enough, then they could diminish the recombination rate of excitons.

Previous studies[60,61] have found that electric fields on the order of 10^7–10^8 V/m significantly affect the exciton recombination oscillator strength and lifetime and can facilitate exciton dissociation. This could explain the observations in our experimental PL

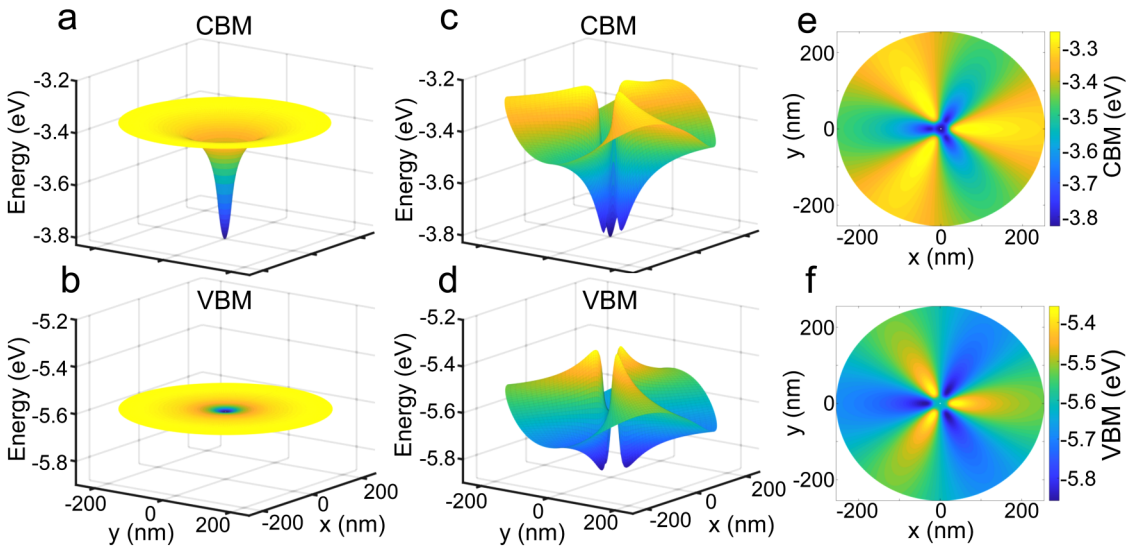

FIG. 9. Depiction of the effect of strain and the piezo-induced electrostatic potential on the spatial distribution of the band edge energies of WSe_2, for the case of a 50 nm indenter radius and a 200 nN indentation load, corresponding to 3.2% maximum strain. (a) The effect of strain on the conduction band minimum and (b) valence band maximum. (c) The effects of strain with the inclusion of piezo-induced electrostatic potential. (e) and (f) are a top-down view of (c) and (d), respectively.

data, which show a lack of redshift beyond ~1% strain. If the region with the largest strain is also experiencing large electric fields and potentials due to the piezoelectric effect, then exciton recombination could be significantly reduced in that region, partially negating the effect of exciton funneling. Previous studies looking at inhomogeneous strain distributions for carrier funneling in TMDs show some indication that the carrier funneling effect might not be as strong as expected. References 9–11 show maximum PL shifts which are all less than 100 meV, implying strains between 0.3% and 0.6%. Reference 10, through scanning tunneling spectroscopy measurements, shows that the bandgap changes locally by an amount consistent with a maximum of 3% biaxial strain, much larger than any PL observations between the references. While this discrepancy is typically attributed to averaging of the signal over an excitation laser spot size larger than the region of high strain, this argument often neglects the presence of carrier funneling, though Ref. 9 shows an agreement between PL shifts and generated strain when accounting for spot size and carrier funneling together. We suggest here that piezoelectrically induced electrostatic potentials can also exert a substantial influence on luminescence behavior in these geometries.

V. SUMMARY AND CONCLUSIONS

We have shown how spatially varying strain can, via the piezoelectric effect, generate electrostatic fields and potentials within monolayer MoS_2 and WSe_2 in the example case of nanoindentation by a spherical indenter. We find that the maximum magnitude of the piezoelectrically induced electrostatic potential is primarily a function of the maximum value of strain and less so a function of the distribution of strain due to tip size. Additionally, we show how the electrostatic potential due to piezoelectricity could be large enough to interfere with exciton drift in the strain field and the carrier funneling mechanism widely cited in the literature. This correlates to the results of our PL experiments from which the strain implied by the redshift is no more than ~1%. This effect could have implications for TMDs in geometries of spatially inhomogeneous strain beyond indentation, such as deformation due to nanopillars.

ACKNOWLEDGMENTS

This research was primarily supported by the National Science Foundation (NSF) through the Center for Dynamics and Control of Materials: An NSF MRSEC under Cooperative Agreement No. DMR-1720595. J.Q. is partially funded by the U.S. Department of Energy (DOE), Office of Basic Energy Sciences under Grant No. DE-SC0019398. Material preparation was funded by the Welch Foundation via Grant No. F-1662. This work was performed in part at the University of Texas Microelectronics Research Center, a member of the National Nanotechnology Coordinated Infrastructure (NNCI), which is supported by the National Science Foundation (Grant No. ECCS-1542159), and using the facilities and instrumentation supported by the National Science Foundation through the Center for Dynamics and Control of Materials: An NSF MRSEC under Cooperative Agreement No. DMR-1720595.

REFERENCES

[1]H. P. Komsa and A. V. Krasheninnikov, Phys. Rev. B. **86**, 241201(R) (2012).
[2]S. Bertolazzi, J. Brivio, and A. Kis, ACS Nano **5**, 9703 (2011).
[3]H. Peelaers and C. G. Van de Walle, Phys. Rev. B **86**, 241401(R) (2012).
[4]P. Johari and V. B. Shenoy, ACS Nano **6**, 5449 (2012).

[5]H. J. Conley, B. Wang, J. I. Ziegler, R. F. Haglund, Jr., S. T. Pantelides, and K. I. Bolotin, Nano Lett. **13**, 3626 (2013).
[6]C.-H. Chang, X. Fan, S.-H. Lin, and J.-L. Kuo, Phys. Rev. B **88**, 195420 (2013).
[7]R. Frisenda, M. Drüppel, R. Schmidt, S. M. de Vasconcellos, D. P. de Lara, R. Bratschitsch, M. Rohlfing, and A. Castellanos-Gomez, npj 2D Mater. Appl. **1**, 10 (2017).
[8]J. Feng, X. Qian, C.-W. Huang, and J. Li, Nat. Photonics **6**, 866 (2012).
[9]A. Castellanos-Gomez, R. Roldan, E. Cappelluti, M. Buscema, F. Guinea, H. S. J. van der Zant, and G. A. Steele, Nano Lett. **13**, 5361 (2013).
[10]H. Li *et al.*, Nat. Commun. **6**, 7381 (2015).
[11]D. F. Cordovilla Leon, Z. Li, S. W. Jang, C.-H. Cheng, and P. B. Deotare, Appl. Phys. Lett. **113**, 252101 (2018).
[12]A. Branny, S. Kumar, R. Proux, and B. D. Gerardot, Nat. Commun. **8**, 15053 (2017).
[13]C. Palacios-Berraquero *et al.*, Nat. Commun. **8**, 15093 (2017).
[14]M. Blauth, M. Jürgensen, G. Vest, O. Hartwig, M. Prechtl, J. Cerne, J. J. Finley, and M. Kaniber, Nano Lett. **18**, 6812 (2018).
[15]M. R. Rosenberger, C. K. Dass, H.-J. Chuang, S. V. Sivaram, K. M. McCreary, J. R. Hendrickson, and B. T. Jonker, ACS Nano **13**, 904 (2019).
[16]W. Wu *et al.*, Appl. Phys. Lett. **114**, 213102 (2019).
[17]K.-A. N. Duerloo, M. T. Ong, and E. J. Reed, J. Phys. Chem. Lett. **3**, 2871 (2012).
[18]W. Wu *et al.*, Nature **514**, 470 (2014).
[19]H. Zhu *et al.*, Nat. Nanotechnol. **10**, 151 (2015).
[20]M. N. Blonsky, H. L. Zhuang, A. K. Singh, and R. G. Hennig, ACS Nano **9**, 9885 (2015).
[21]D. L. Smith, Solid State Commun. **57**, 919 (1986).
[22]T. F. Kuech, R. T. Collins, D. L. Smith, and C. Mailhiot, J. Appl. Phys. **67**, 2650 (1990).
[23]E. T. Yu, G. J. Sullivan, P. M. Asbeck, C. D. Wang, D. Qiao, and S. S. Lau, Appl. Phys. Lett. **71**, 2794 (1997).
[24]T. Takeuchi, S. Sota, M. Katsuragawa, M. Komori, H. Takeuchi, H. Amano, and I. Akasaki, Jpn J. Appl. Phys. **236**, L382 (1997).
[25]S. F. Chichibu *et al.*, Appl. Phys. Lett. **73**, 2006 (1998).
[26]E. T. Yu, X. Z. Dang, P. M. Asbeck, S. S. Lau, and G. J. Sullivan, J. Vac. Sci. Technol. B **17**, 1742 (1999).
[27]O. Ambacher *et al.*, J. Appl. Phys. **85**, 3222 (1999).
[28]J. Qi, Y.-W. Lan, A. Z. Stieg, J.-H. Chen, Y.-L. Zhong, L.-J. Li, C.-D. Chen, Y. Zhang, and K. L. Wang, Nat. Commun. **6**, 7430 (2015).
[29]A. Weston *et al.*, "Atomic reconstruction in twisted bilayers of transition metal dichalcogenides," Nat. Nanotechnol. (published online, 2020).
[30]J. C. Hulteen and R. P. Van Duyne, J. Vac. Sci. Technol. A **13**, 1553 (1995).
[31]X. H. Li, P. C. Li, D. Z. Hu, D. M. Schaadt, and E. T. Yu, J. Appl. Phys. **114**, 044310 (2013).
[32]P.-C. Li and E. T. Yu, J. Opt. Soc. Am. B **30**, 2584 (2013).
[33]P.-C. Li and E. T. Yu, J. Appl. Phys. **114**, 133104 (2013).
[34]X. Li, P.-C. Li, L. Ji, C. Stender, S. R. Tatavarti, K. Sablon, and E. T. Yu, Sol. Energy Mater. Sol. Cells **143**, 567 (2015).
[35]A. Castellanos-Gomez, M. Buscema, R. Molenaar, V. Singh, L. Janssen, H. S. J. van der Zant, and G. A. Steele, 2D Mater. **1**, 11002 (2014).
[36]C. Lee, H. Yan, L. E. Brus, T. F. Heinz, J. Hone, and S. Ryu, ACS Nano **4**, 2695 (2010).
[37]H. Li, Q. Zhang, C. C. R. Yap, B. K. Tay, T. H. T. Edwin, A. Olivier, and D. Baillargeat, Adv. Funct. Mater. **22**, 1385 (2012).
[38]W. Zhao, Z. Ghorannevis, K. K. Amara, J. R. Pang, M. Toh, X. Zhang, C. Kloc, P. H. Tan, and G. Eda, Nanoscale **5**, 9677 (2013).
[39]P. Tonndorf *et al.*, Opt. Express **21**, 4908 (2013).
[40]J. E. Sader, J. W. M. Chon, and P. Mulvaney, Rev. Sci. Instrum. **70**, 3967 (1999).
[41]A. Föppl, Vor. über Tech. Mech. **5**, 132 (1907).
[42]H. Hencky, Z. Math. Phys. **63**, 311 (1915).
[43]N. M. Bhatia and W. Nachbar, Int. J. Nonlinear Mech. **3**, 307 (1968).
[44]E. Schwerin, ZAMM **9**, 482 (1929).
[45]M. R. Begley and T. J. Mackin, J. Mech. Phys. Solids **52**, 2005 (2004).
[46]C. Jin, A. Davoodabadi, J. Li, Y. Wang, and T. Singler, J. Mech. Phys. Solids **100**, 85 (2017).
[47]J. L. Feldman, J. Phys. Chem. Solids **37**, 1141 (1976).
[48]J. Kang, S. Tongay, J. Zhou, J. Li, and J. Wu, Appl. Phys. Lett. **102**, 012111 (2013).
[49]R. Zhang, V. Koutsos, and R. Cheung, Appl. Phys. Lett. **108**, 042104 (2016).
[50]S. M. Kogan, Sov. Phys. Solid State **5**, 2069 (1964).
[51]C. J. Brennan, R. Ghosh, K. Koul, S. K. Banerjee, N. Lu, and E. T. Yu, Nano Lett. **17**, 5464 (2017).
[52]C. J. Brennan, K. Koul, N. Lu, and E. T. Yu, Appl. Phys. Lett. **116**, 053101 (2020).
[53]L. N. Dworsky, *Introduction to Numerical Electrostatics Using MATLAB* (Wiley, Hoboken, NJ, 2014), pp. 51–64.
[54]U. Komaragiri, M. R. Begley, and J. G. Simmonds, J. Appl. Mech. **72**, 203 (2005).
[55]J. W. Christopher, B. B. Goldberg, and A. K. Swan, Sci. Rep. **7**, 14062 (2017).
[56]T. Godde *et al.*, Phys. Rev. B **94**, 165301 (2016).
[57]D. Lloyd, X. Liu, J. W. Christopher, L. Cantley, A. Wadehra, B. L. Kim, B. B. Goldberg, A. K. Swan, and J. S. Bunch, Nano Lett. **16**, 5836 (2016).
[58]O. B. Aslan, M. Deng, and T. F. Heinz, Phys. Rev. B **98**, 115308 (2018).
[59]J. Wiktor and A. Pasquarello, Phys. Rev. B **94**, 245411 (2016).
[60]B. Scharf, T. Frank, M. Gmitra, J. Fabian, I. Žutić, and V. Perebeinos, Phys. Rev. B **94**, 245434 (2016).
[61]M. Massicotte *et al.*, Nat. Commun. **9**, 1633 (2018).